

# High-Resolution Nuclear Magnetic Resonance Spectroscopy With Picomole Sensitivity by Hyperpolarisation On A Chip

James Eills,<sup>†,‡</sup> William Hale,<sup>†,‡</sup> Manvendra Sharma,<sup>†</sup> Matheus Rossetto,<sup>†,¶</sup> Malcolm H. Levitt,<sup>†</sup> and Marcel Utz<sup>\*,†</sup>

<sup>†</sup>*School of Chemistry, University of Southampton, United Kingdom*

<sup>‡</sup>*These authors contributed equally to this work*

E-mail: marcel.utz@soton.ac.uk

## Abstract

We show that high-resolution NMR can reach picomole sensitivity for micromolar concentrations of analyte by combining parahydrogen induced hyperpolarisation (PHIP) with a high-sensitivity transmission line micro-detector. The para-enriched hydrogen gas is introduced into solution by diffusion through a membrane integrated into a microfluidic chip. NMR microdetectors, operating with sample volumes of a few  $\mu\text{L}$  or less, benefit from a favourable scaling of mass sensitivity. However, the small volumes make it very difficult to detect species present at less than millimolar concentrations in microfluidic NMR systems. In view of overcoming this limitation, we implement parahydrogen-induced polarisation (PHIP) on a microfluidic device with 2.5  $\mu\text{L}$  detection volume. Integrating the hydrogenation reaction into the chip minimises polarisation losses to spin-lattice relaxation, allowing the detection of picomoles of substance. This corresponds to a concentration limit of detection of better than  $1 \mu\text{M}\sqrt{s}$ , unprecedented at this sample volume. The stability and sensitivity of the system allows quantitative characterisation of the signal dependence on flow rates and other reaction parameters and permits homo- ( $^1\text{H}$ - $^1\text{H}$ ) and heteronuclear ( $^1\text{H}$ - $^{13}\text{C}$ ) 2D NMR experiments at natural  $^{13}\text{C}$  abundance.

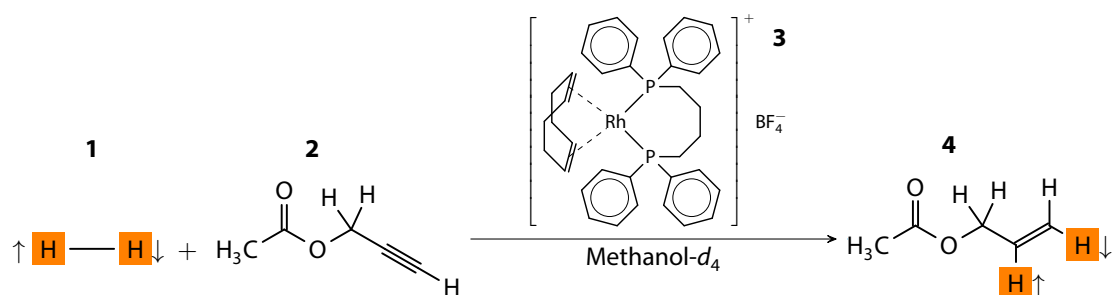


Figure 1: Scheme of the reaction used in the PHIP@chip experiment. Hydrogen gas **1** enriched in parahydrogen reacts with propargyl acetate **2** in the presence of the Rh catalyst **3** to form allyl acetate **4**.

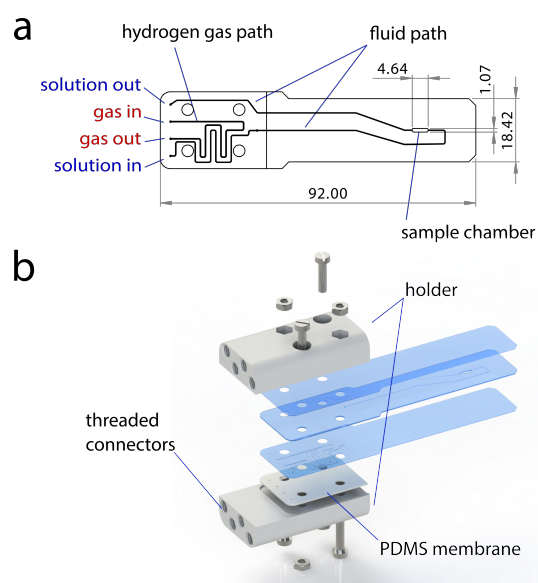


Figure 2: Overview of the PHIP@chip device. a: outline drawing of the chip (dimensions in mm). b: CAD rendering of the chip assembly with individual chip layers separated, consisting of the PMMA chip, PDMS membrane, and two 3D printed holders with threads for the gas and fluid connections. The hydrogen gas diffuses through the PDMS membrane into the flowing liquid.

## Introduction

High-resolution NMR spectroscopy is a superbly versatile method which provides detailed and quantitative information on chemical composition and structure. It is widely used to follow the progress of chemical reactions,<sup>1</sup> as well as metabolic processes in living systems.<sup>2</sup> However, NMR suffers from inherently low sensitivity, which is due in part to the very weak polarisation of nuclear spins along the magnetic field for samples in thermal equilibrium at ambient conditions. Conventional high-resolution NMR therefore requires nanomole quantities of sample. Many important problems require detection of analytes at low micromolar concentrations, such as transient reaction intermediates, or metabolic species. Despite the comparatively higher mass sensitivity of NMR for small sample volumes,<sup>3,4</sup> conventional micro-NMR systems around 1  $\mu\text{L}$  achieve mass limits of detection of no better than<sup>5</sup>  $1 \text{ nmol}\sqrt{s}$ , corresponding to a concentration limit of detection of  $1 \text{ mM}\sqrt{s}$ . An increase of several orders of magnitude in sensitivity is therefore required to enable NMR studies of mass-limited samples at micromolar concentrations.

Microfluidic lab-on-a-chip devices are finding increasing applications in chemistry and the life sciences. They provide detailed control over the experimental conditions at a much smaller length scale than conventional reactors, and allow integration of synthesis, separation, and analytical steps on a single platform.<sup>6</sup> The small size also affords the possibility of high experimental throughput. In the life sciences, microfluidic devices are increasingly used as sophisticated culture platforms for cells, cell assemblies, tissues, and small organisms.<sup>7</sup> The integration of NMR with microfluidics<sup>5,8-11</sup> is promising, as it enables in-situ, non-invasive monitoring of chemical and metabolic processes in lab-on-a-chip systems.

The usefulness of microfluidic NMR could therefore be significantly enhanced if the following conditions could be met: (i) sample volumes around 1  $\mu\text{L}$  or less; (ii) a concentration limit of detection near  $1 \mu\text{M}\sqrt{s}$ ; and (iii) spectral resolution of better than 0.01 ppm to allow distinction and identification of chemical species.

Although exquisitely sensitive NMR detection schemes exist at low magnetic fields, approaching even single-spin detection in favourable cases,<sup>12</sup> they lack spectral resolution. While a recent study has demonstrated resolution of  $J$  couplings using a nitrogen-vacancy (NV) centre

magnetometer,<sup>13</sup> none of these alternative detection schemes are compatible with high (several Tesla) magnetic fields, which are essential to produce spectral dispersion by chemical shifts. So far, no method has been demonstrated with the combination of high spectral resolution, high chemical dispersion, and high sensitivity for small volumes required for advanced microfluidic NMR measurements significantly below the 1 mM concentration scale.

Hyperpolarisation methods generate substances which exhibit a transiently high level of nuclear spin polarisation, much larger than thermal equilibrium. As a result, hyperpolarised substances can give NMR signals that are enhanced by more than 4 orders of magnitude.<sup>14</sup> Hyperpolarisation methods can be combined with micro-NMR detectors and microfluidic systems.<sup>15–22</sup> One such method involves the chemical reaction of the singlet spin isomer of molecular hydrogen, and is called parahydrogen-induced hyperpolarisation (PHIP).<sup>23–26</sup>

While most studies have so far brought the reaction liquid in direct contact with hydrogen gas either through bubbling or by atomisation of the liquid in a hydrogen-filled chamber,<sup>27–33</sup> liquid-gas interfaces (and bubbles in particular) pose difficulties in the context of microfluidic devices, since they tend to alter the flow properties, and can block fluid transport altogether. Continuous delivery of parahydrogen by diffusion through gas-permeable membranes has been demonstrated at conventional size scales.<sup>34,35</sup> It has been shown that silicone elastomer membranes can be used to deliver parahydrogen directly to a flowing liquid in a microfluidic device.<sup>21</sup> Bordonali et al<sup>22</sup> have recently combined a microfluidic NMR probe system with a gas exchange chip based on a silicone elastomer membrane to implement the SABRE (signal enhancement by reversible exchange) variant of parahydrogen-induced polarisation, but achieved only small signal enhancement factors (3 to 4).

In distinction from previous work,<sup>27–33,35</sup> we integrate the hydrogenation reactor into the chip itself, which greatly reduces the polarisation losses due to spin-lattice relaxation. As shown below, we achieve a signal enhancement factor over thermal polarisation of about 1800, allowing detection of a picomole quantity of analyte in a sample volume of 2.5  $\mu\text{L}$ , while maintaining the full resolution of conventional  $^1\text{H}$  NMR spectroscopy.

This is accomplished by letting the parahydrogen gas diffuse through a silicone elastomer membrane<sup>35</sup> to come into contact with a solution flowing through the chip at a constant rate.

The solution contains a precursor, which is hydrogenated through a homogeneous catalyst also present in the solution. The microfluidic device is held in the bore of a conventional NMR magnet using a purpose-built transmission line NMR probe. This yields a continuous on-chip stream of hyperpolarised material. As shown in the following, in addition to very high detection sensitivities, this also results in a continuous and highly stable operation of the system, making it possible to perform hyperpolarised two-dimensional NMR experiments.<sup>34,36–38</sup> By replacing the hyperpolarised gas feed with hydrogen gas at thermal equilibrium, it is possible to gain kinetic information on the hydrogenation process, as well as to calibrate the intensity of the hyperpolarised NMR signals. This allows accurate assessment of the achieved polarisation levels, something that has been notoriously difficult in the context of parahydrogen-induced polarisation.

## Experimental

The microfluidic chips were constructed from three layers of cell cast poly(methyl methacrylate) (PMMA) sheet material (Weatherall Equipment). The sheet thickness was 200  $\mu\text{m}$  for the top and bottom layers, and 500  $\mu\text{m}$  for the middle layer. The fluid and gas channels were designed on AutoCAD and cut into the PMMA using a laser cutter (HPC Laser L3040) to a width and depth of 150  $\mu\text{m}$ . The layers were subsequently bonded together with a plasticiser (2.5% v/v dibutyl phthalate in isopropyl alcohol) under heat and pressure (358 K, 3.5 tonnes).<sup>39</sup> The total internal fluid volume is 4  $\mu\text{L}$ , and the sample chamber is 2.5  $\mu\text{L}$ .

The device also employs a poly(dimethyl siloxane) (PDMS) membrane (Shielding Solutions) to facilitate para- $\text{H}_2$  transport, of 1 mm thickness with laser-cut screw holes. The parahydrogen polarisation lifetime in the PDMS after  $\text{O}_2$  removal was measured to be  $\sim 4$  h (see supplementary information). The PMMA chip and PDMS membrane layer are sealed with a pair of screw-tightened 3D printed (Accura Xtreme, Proto Labs) holders, with fluid and gas in/out ports (to fit Kinesis UK NanoPorts).

The assembled microfluidic device was put in a transmission line based home-built probe.<sup>11</sup> The device sits between the two detector planes with the sample chamber of the device aligned

with the sensitive area of the detector. All NMR experiments were performed at a field strength of 11.7 T with an AVANCE III console. Nutation frequencies for RF pulses were 100 kHz for protons, and 20 kHz for carbon in the case of the HMQC spectrum. 16k data points were acquired over 1.2 s for proton 1D spectra. Saturation recovery experiments used a train of 512  $\pi/2$  pulses separated by a delay of 0.1 ms, followed by a recovery delay, and a  $\pi/4$  excitation pulse. The PH-TOCSY spectrum was acquired using the States-TPPI method, with 256  $t_1$  increments, averaging 8 transients per increment. 2048 complex data points in 0.2 s were acquired for each increment. The PH-HMQC experiment was acquired using the States method, with 128  $t_1$  increments, averaging 8 transients with 2048 complex points over 0.2 s. 1D spectra were processed using MestreNova (Mestrelab, Italy). 2D spectra were processed using scripts written in Julia.<sup>40</sup>

To generate parahydrogen gas at 50% para enrichment, hydrogen gas (purity 99.995%) was passed through a home-built parahydrogen generator containing an iron (III) oxide catalyst cooled to 77 K using liquid nitrogen.

The solution before reaction contained 20 mM propargyl acetate **2** and 5 mM 1,4-bis(diphenylphosphino)butane(1,5-cyclooctadiene)rhodium tetrafluoroborate **3** in methanol- $d_4$ . In an attempt to avoid possible spin relaxation or chemical side-reaction effects, dissolved oxygen from the atmosphere was removed by 5 minutes of vigorous helium bubbling.

The parahydrogen gas was delivered through a PTFE tube (1/16 inch O.D., 1/32 inch I.D.) into the 3D printed chip holder, and out via a second PTFE line, using a mass flow controller (Cole-Parmer) to limit the flow to 20 mL min<sup>-1</sup> at an overpressure of 5 bar. Although most of the parahydrogen gas passes directly through the system, some amount dissolves into the PDMS layer, which in terms of H<sub>2</sub> solubility behaves similarly to other organic solvents. The solution was loaded into a 3.5 mL plastic syringe with a Luer lock connection to in-flow PEEK tubing (1/16 inch O.D., 0.007 inch I.D.) leading to the chip. The same tubing was used for the solution out-flow into a container exposed to a back pressure of 1.5 bar of nitrogen gas, to prevent formation of hydrogen bubbles in the chip. Solution flow into the chip was controlled with a syringe pump (Cole-Parmer).

## Results and Discussion

The hydrogenation reaction system employed in the present work is shown in Fig. 1. Para-hydrogen-enriched hydrogen gas **1** was allowed to react with propargyl acetate **2**, in the presence of a rhodium catalyst **3**. The substrate **2** was chosen in view of future studies based on side-arm hydrogenation.<sup>31,32,41</sup>

Fig. 2 shows the microfluidic device used for the present study. It consists of a chip made from PMMA, which houses a sample chamber of 2.5  $\mu\text{L}$  volume that aligns with the transmission line detector of a home-built NMR probe assembly, which was fitted inside of an 11.7 T NMR magnet. Fluid is flowed through the chip by means of a syringe pump installed outside of the magnet bore; connections are made through threaded ports in the two 3D-printed holders shown in Fig. 2b. Para-enriched  $\text{H}_2$  gas at 5 bar above ambient pressure flows through a second channel in the chip, which runs in the immediate vicinity of the liquid channel (a depiction of the set-up is given in the SI).

The chip consists of three laser-cut layers of poly methylmethacrylate (PMMA) bonded together, as shown in Fig. 2b. Channels in the left part of the chip, where it is clamped between the holders, are cut through the top layer, while they are scored into the middle layer of the chip (and hence sealed from the outside) in the free part of the device. Within the clamps, the exposed channels are sealed by means of a PDMS membrane. The flowing liquid as well as the pressurised hydrogen gas are therefore exposed to the PDMS layer, which serves as a diffusion bridge for the hydrogen. The holders, made by 3D printing, keep the membrane and the chip aligned, and maintain mechanical pressure to ensure sealing. Channels inside the holders guide the fluid and gas to and from the four access points at the top end of the chip, as shown in Fig. 2b. The PDMS membrane acts both as a diffusion conduit for hydrogen gas and as a fluid seal. In a crucial difference to the otherwise similar geometry of the hydrogenation chip used by Bordonali et al,<sup>22</sup> the gas and liquid channels are arranged side by side, and molecular hydrogen diffuses through the bulk of the PDMS material rather than across the membrane. Clamping the PDMS membrane onto the chip using the holders, this makes it possible to use large gas pressures (up to 5 bar in the present experiments). This would be difficult to achieve if the liquid and gas channels were arranged on opposite sides of the membrane.

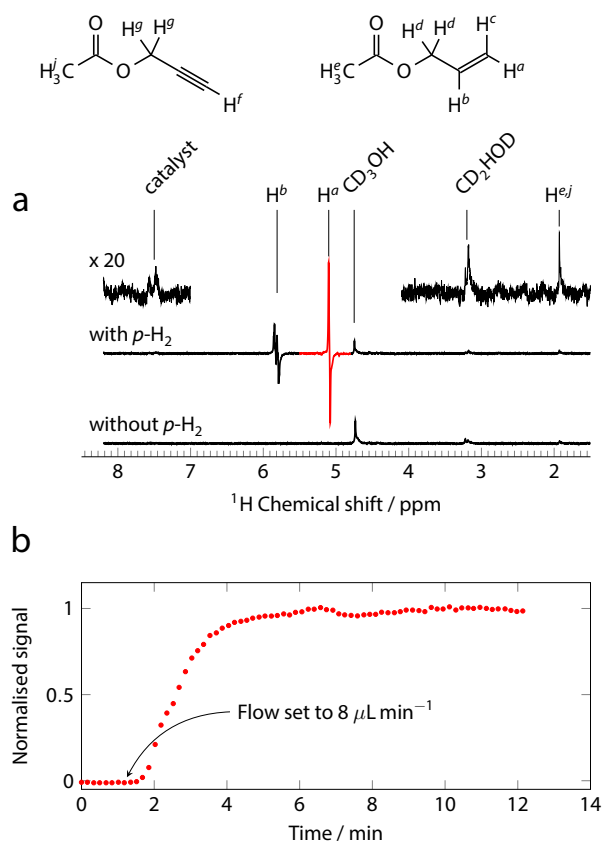


Figure 3: a: Single-scan proton NMR spectrum obtained with parahydrogen at 5 bar using the PHIP@chip setup at a continuous flow rate of  $8 \mu\text{L min}^{-1}$  (top trace with enlargement). Antiphase doublets from the two hyperpolarised protons  $\text{H}^a$  and  $\text{H}^b$  are clearly visible at 5.2 ppm and 5.9 ppm, respectively. Without parahydrogen, these signals are not observed (bottom trace). b: Buildup of the hyperpolarised signal ( $\text{H}^a$ ) after initiation of flow.



Fig. 3a shows a single-scan proton NMR spectrum obtained from a steady-state PHIP@chip experiment (top trace), compared to the spectrum obtained without parahydrogen (bottom trace). The hyperpolarised spectrum is dominated by an antiphase doublet, centred at 5.17 ppm, and an antiphase multiplet at 5.92 ppm, corresponding to protons in the H<sup>a</sup> and H<sup>b</sup> positions of the hydrogenation product **4**. The PDMS membrane is equilibrated with para-enriched hydrogen gas, which is supplied from an aluminium storage tank at a regulated pressure of 5 bar. The gas flow rate is kept constant at 20 mL min<sup>-1</sup> by means of a mass flow controller placed after the chip. This ensures that the gas channel always contains fresh para-enriched hydrogen gas at the design pressure of 5 bar. The fluid channel of the chip is pre-filled with a solution of 20 mM precursor **2** and 5 mM catalyst **3** in methanol-*d*<sub>4</sub>. NMR spectra are acquired every 30 s, using a  $\pi/4$  excitation pulse. The fluid channel is connected to a syringe pump situated outside the NMR magnet. The liquid flow is started by setting the target flow rate on the syringe pump to 8  $\mu\text{L min}^{-1}$  (marked by an arrow Fig. 3b). The NMR signal intensity begins to rise about 30 s later, and reaches a steady state after about two minutes.

The hydrogen transport through the membrane and its uptake into the flowing liquid was simulated using two coupled finite element models: a dilute species diffusion model for hydrogen gas in the PDMS membrane, and a dilute species diffusion and convection model for hydrogen dissolved in the flowing liquid. The hydrogen partial pressures at the liquid/PDMS interface are constrained to be equal, and the hydrogen partial pressure at the gas/PDMS interface was set to a fixed value of 5 bar. Fig. 4a shows the diffusive flux of hydrogen through the PDMS membrane. Since the gas/PDMS interface acts as a source, and the liquid/PDMS interface as a sink for hydrogen, the flux is strongest where the two channels are in close proximity. At the lowest flow rate, significant transport only takes place in a very small area, and the liquid is saturated with hydrogen within the first few mm of the path which is in contact with the PDMS. The higher the flow rate, the further the area of significant flux extends downstream. At about 10  $\mu\text{L min}^{-1}$ , the hydrogen flux covers the entire length of the area between the liquid and gas channel interfaces. The finite element model also predicts the resulting concentration of hydrogen in the liquid (methanol) as a function of flow rate. This is shown by the solid line in Fig. 4b. The circles represent NMR measurements. At flow rates between 2 and

$10 \mu\text{Lmin}^{-1}$ , experimental results are in good agreement with the simulation. At higher flow rates, however, the experimentally observed hydrogen concentrations are significantly lower than the predictions. It is currently unclear what causes this discrepancy; possibly high flow rates lead to deformation of the PDMS layer over the liquid channel and thus change the uptake geometry. At flow rates below  $10 \mu\text{Lmin}^{-1}$ , the simulation and experiments both indicate that the flowing solvent is nearly saturated with hydrogen. Detailed information on the finite element simulations, as well as data on parahydrogen partial pressure throughout the chip is given in the supporting information.

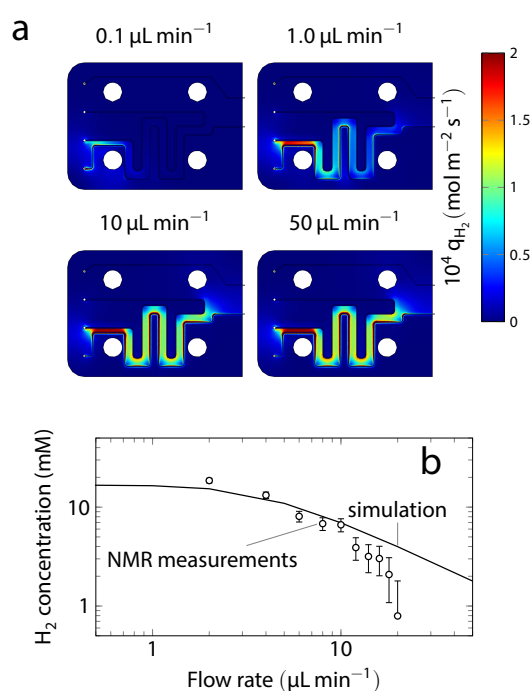


Figure 4: Finite element simulation of hydrogen uptake. a: Diffusive hydrogen flux in the PDMS membrane for different liquid flow rates; b: final hydrogen concentration in flowing methanol as a function of flow rate. Solid line: simulation, open circles: NMR measurements.

Clearly, the steady-state signals observed at constant flow rate are the result of a dynamic equilibrium between the rate of hydrogenation, the rate of transport of the hydrogenated product to the sample chamber and its removal from it, and spin-lattice relaxation. In order to probe the interplay of these factors, the NMR signal was suppressed by saturating the spin populations with a train of  $512 \pi/2$  pulses separated by  $100 \mu\text{s}$  delays. The signal intensity was then measured as a function of the delay between the end of the saturation train and the NMR excitation pulse. Fig. 5a shows an example of the data thus obtained at a flow rate  $q = 8 \mu\text{Lmin}^{-1}$

(results for other flow rates are given in the SI). The signal increases rapidly after saturation, reaching steady-state levels after about 10 s.

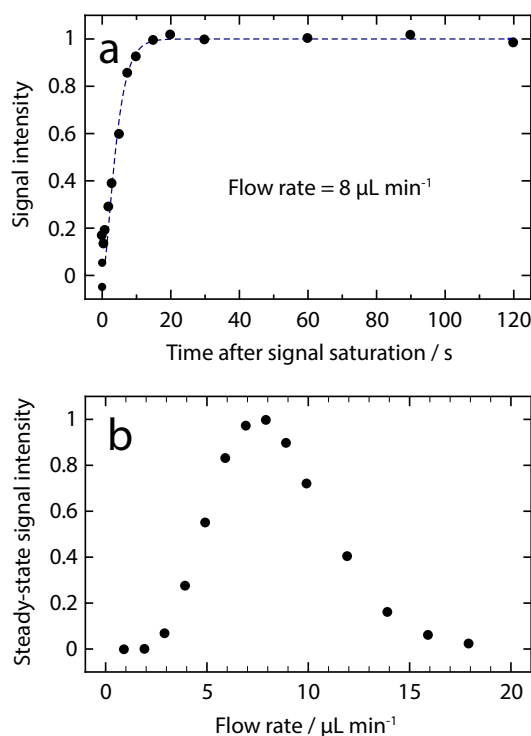


Figure 5: Saturation recovery results. a: Signal buildup at constant flow rate after saturation (solid dots: measured data points, the dashed line is a guide to the eye); b: Magnitude of the steady-state signal after full recovery (at least 100 s after saturation) as a function of flow rate. A clear maximum at 8  $\mu\text{L min}^{-1}$  is observed.

The intensity of the steady-state NMR signal exhibits a clear maximum with flow rate (Fig. 5b), reflecting a balance between hydrogen uptake, reaction kinetics, and spin-lattice relaxation. The optimum, with the largest signal at saturation, is reached at a flow rate of 8  $\mu\text{L min}^{-1}$ . The nature of the stationary state established in the system at each flow rate becomes clearer if the saturation recovery data is plotted in terms of the volume displaced during the saturation recovery time  $q\tau$ , rather than the recovery time itself, and normalised to the steady-state signal intensity at each flow rate, as shown in Fig. 6. At flow rates below the intensity maximum at  $q < 8 \mu\text{L min}^{-1}$  (solid circles), the data points collapse onto a curve that shows an initial linear increase up to a displaced volume of about 1  $\mu\text{L}$ , followed by rapid saturation to the steady-state value. This behaviour clearly indicates that the signal recovery in this regime is dominated by the convective fluid transport. At these flow rates, a constant concentration of hyperpolarised material is established in the flowing liquid upstream of the

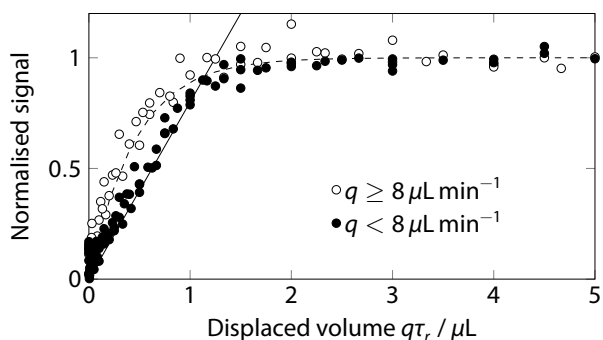


Figure 6: Signal recovery after saturation, normalised by the maximum signal observed at long recovery times. The horizontal axis is the volume moved through the chip during the recovery time  $\tau_r$ , i.e.,  $q\tau_r$ , where  $q$  is the flow rate. Filled circles correspond to flow rates below the optimum ( $q < 8 \mu\text{L min}^{-1}$ ), whereas open circles are obtained at flow rates  $q \geq 8 \mu\text{L min}^{-1}$ . The solid and dashed lines are guides to the eye for the solid and open circle data points, respectively.

sample chamber, and is simply carried back into view of the NMR detector after the saturation pulses end. The maximum signal is reached after a volume of about  $1.5 \mu\text{L}$  has been displaced. This is less than the capacity of the sample chamber, reflecting the uneven velocity distribution inside it. At flow rates above the optimum ( $q \geq 8 \mu\text{L min}^{-1}$ ), a somewhat different behaviour is observed. The initial recovery rate is faster (Fig. 6, open circles), and appears to follow an exponential rather than linear shape. This suggests that at these flow rates, the stationary state is not yet established at the point where the liquid enters the sample chamber, and therefore, the observed recovery is dominated by the ongoing hydrogenation reaction. A detailed kinetic analysis of these processes is beyond the present scope, but is underway in our laboratory, and will be reported on a later occasion.

In order to determine the sensitivity of detection of the hydrogenation product at the optimum flow rate, the experiment was repeated using normal hydrogen. In this case, the signal from protons  $\text{H}^a$  and  $\text{H}^b$  of the hydrogenation product **4** are too weak to be observed above the noise in a single scan. Fig. 7 compares the hyperpolarised signal (a) to the averaged signal of 512 transients obtained with hydrogen in thermal equilibrium (b).

Since the methyl group in the precursor and the hydrogenation product contribute to the same signal at 2.05 ppm (signal labelled  $\text{H}^{e,j}$  in Fig. 3a), this signal can be used as a calibration standard, with a concentration of 20 mM which is unaffected by the hydrogenation reaction.

By comparing this integral to that of the signal from the  $H^a$  protons, the concentration of hydrogenated product can be quantified. At a flow rate of  $8 \mu\text{L min}^{-1}$ , an allyl acetate (product) concentration of  $(0.29 \pm 0.05) \text{ mM}$  was found, corresponding to a total of  $(0.725 \pm 0.125) \text{ nmol}$  in the  $2.5 \mu\text{L}$  sample volume.

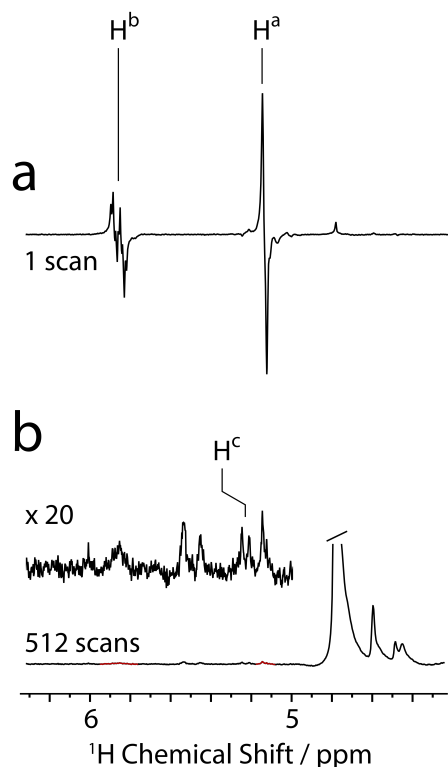


Figure 7: a: Single-scan steady-state spectrum obtained at the optimum flow rate with para-enriched  $\text{H}_2$ ; b: spectrum obtained at the same flow rate with hydrogen gas in thermal equilibrium. 512 transients have been averaged. Signal enhancement by PHIP was determined by comparing the integral of the positive lobe of the  $H^a$  signal in spectrum a to the integral of the corresponding (purely absorptive) peak in spectrum b. A fully labelled spectrum is given in the SI.

This quantity can be used to determine the limit of detection of the hyperpolarised product. The signal/noise ratio (SNR) in the spectrum shown in Fig. 7a is  $400(\pm 10\%)$ , and the line width is  $6 \pm 0.5 \text{ Hz}$ . The normalised limit of detection is given by

$$\text{nLOD}_\omega = \frac{3n}{\text{SNR} \sqrt{\Delta f}}, \quad (1)$$

where  $n$  is the amount of sample and  $\Delta f$  is the signal bandwidth. In the present case, one finds  $\text{nLOD}_\omega = (2.2 \pm 0.4) \text{ pmol} \sqrt{\text{s}}$ . Limits of detection in this range have so far only been

reported in very limited circumstances, including chemically-induced dynamic nuclear polarisation (CIDNP),<sup>42</sup> or by making use of unconventional low-field detection systems such as force-detected magnetic resonance or optical detection methods.<sup>12</sup> In the present case, we are using conventional inductive detection, and retain the full resolution and specificity that make high-field proton NMR spectroscopy such a powerful analytical tool.

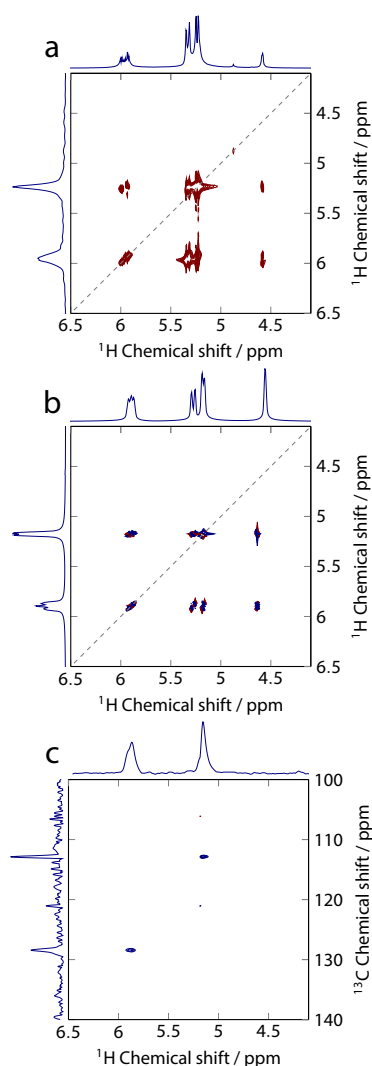


Figure 8: The continuous flow PHIP@chip approach allows acquisition of two-dimensional spectra with very high sensitivity. a: PH-TOCSY spectrum of the hyperpolarised reaction mixture, flowing at  $8 \mu\text{L min}^{-1}$ . b: Simulated PH-TOCSY spectrum. The diagonal in the spectrum is marked by a dashed grey line. Only the protons originating from parahydrogen give signals on the diagonal; the polarisation is transferred to the other locations by the isotropic mixing sequence. Both PH-TOCSY spectra are plotted in magnitude mode (phase sensitive spectra are given in the SI). c:  $^1\text{H}$ - $^{13}\text{C}$  PH-HMQC spectrum showing two separate multiplets, each correlating one of the two hyperpolarised protons with the directly bonded  $^{13}\text{C}$  spin.

The mass limit of detection (LOD) for protons at a magnetic field of 14.1 T (corresponding

to a proton Larmor frequency of 600 MHz) in state-of-the-art commercial NMR probes with a conventional sample volume of 0.5 mL is approximately  $100 \text{ nmol} \sqrt{\text{s}}$ . Microfluidic NMR systems can make use of miniaturised NMR detectors, which benefit from a favourable scaling of the mass sensitivity with detection volume.<sup>3,9,43</sup> At a size scale of  $2.5 \mu\text{L}$ , a mass sensitivity around  $1 \text{ nmol} \sqrt{\text{s}}$  has been reported.<sup>5</sup> However, due to the limited volume in such systems, the *concentration* sensitivity is very poor, such that only compounds present at mM levels can be quantified in microfluidic NMR systems. This situation gets worse as the detector volume decreases. By contrast, many samples of interest, such as metabolites in microfluidic culture systems, are only present at  $\mu\text{M}$  levels. In the present case, the concentration limit of detection is

$$\text{cLOD}_\omega = \frac{\text{nLOD}_\omega}{V} = (0.88 \pm 0.16) \mu\text{M} \sqrt{\text{s}}. \quad (2)$$

From the ratio of the signal intensities in the thermal and hyperpolarised spectra shown in Fig. 7a and b, it is possible to estimate the  $^1\text{H}$  polarisation levels. In the thermal spectrum, the SNR is about 5:1, whereas it is 400:1 in the hyperpolarised spectrum. The thermal spectrum is obtained from 512 transients, therefore the single transient thermal SNR would be  $5/\sqrt{512} \approx 0.22$ . This leads to a signal enhancement factor of  $\varepsilon \approx 400/0.22 \approx 1800$ .

This can be compared to the expected signal enhancement given the enrichment level of para-hydrogen used in the experiment. The ideal enhancement factor is given by

$$\varepsilon_{id} = \frac{4x_p - 1}{3} \frac{1}{\sqrt{2}} \frac{k_B T}{\hbar \gamma B_0}, \quad (3)$$

where  $x_p$  is the mole fraction of parahydrogen in the feed gas,  $\gamma$  is the magnetogyric ratio,  $B_0$  is the magnetic field, and  $\hbar$  and  $k_B$  are Planck's and Boltzmann's constants, respectively. The factor  $\frac{1}{\sqrt{2}}$  reflects the use of a  $\pi/4$  pulse for the hyperpolarised experiment. At a temperature of  $T = 298 \text{ K}$  and a magnetic field of  $11.7 \text{ T}$ , and with  $x_p = 0.5$ , this yields  $\varepsilon_{id} \approx 5900$ , which is a factor of 3.3 larger than the experimentally observed enhancement factor. We can therefore conclude that about  $2/3$  of the theoretically available spin order is lost to relaxation under the present experimental conditions.

A great advantage of the continuously operating microfluidic PHIP system is the ability

to acquire many transients in succession under virtually unchanged conditions. This is difficult to achieve with bubbling hydrogen through a solution. As a consequence, hyperpolarised multi-dimensional NMR spectra<sup>34,36–38,44,45</sup> have been recorded either using automated reactors combined with NMR flow probes,<sup>37,38</sup> or using ultrafast acquisition techniques.<sup>36,44,45</sup>

The PHIP@chip setup allows straightforward acquisition of 2D spectra, using conventional  $t_1$  incrementation. To demonstrate this, we have taken 2D TOCSY (Total Correlation Spectroscopy) and HMQC (Heteronuclear Multiple Quantum Coherence) NMR spectra of the reaction mixture at a flow rate of  $8 \mu\text{L min}^{-1}$ . The conventional pulse sequences were modified by replacing the initial  $\pi/2$  pulse with a  $\pi/4$  pulse; we refer to these experiments as “PH-TOCSY” (parahydrogen TOCSY) and “PH-HMQC” (parahydrogen HMQC).

A PH-TOCSY spectrum acquired in 20 min is shown in Fig. 8a. A *thermal equilibrium* TOCSY spectrum of this compound would be expected to contain diagonal peaks connecting the identical nuclear spins in the two acquisition dimensions, and off-diagonal peaks connecting  $J$ -coupled spins. In the PH-TOCSY experiment, the diagonal peaks only appear for the two parahydrogen proton signals, because they are the only spins significantly polarised in the indirect dimension. The other protons are only polarised during the isotropic spin-mixing step of the pulse sequence, and hence do not appear in the indirect dimension. These protons only produce off-diagonal peaks, connecting them to the parahydrogen pair. As shown in Fig. 8b, the simulated spectrum closely corresponds to the experimentally observed one.

A PH-HMQC spectrum acquired in 60 min is shown in Fig. 8c. It contains two peaks, linking the parahydrogen protons to the  $^{13}\text{C}$  spins to which they have a direct  $^1J_{\text{CH}}$  coupling. An experiment of this kind, in which signals are detected at full natural abundance of the  $^{13}\text{C}$  spins (about 1%) in a  $2.5 \mu\text{L}$  detection volume, is only possible due to both the high polarisation levels and stability of the system. The sensitivity of the HMQC spectrum is limited by  $t_1$  noise, due to imperfect cancellation of the signals from molecular sites without  $^{13}\text{C}$ . To some extent, this may stem from residual instability of the flow conditions, as well as temperature fluctuations in the system. It may therefore be possible to improve the sensitivity further by optimising the setup.

The results in Fig. 8 show that the hyperpolarised spin order can be spread to other protons



in the molecule by the application of the isotropic mixing sequence MLEV-17<sup>46</sup> prior to 1D signal acquisition. This simple trick allows one to hyperpolarise any protons that are *J*-coupled to the parahydrogen pair, which makes the technique more general.

Much ongoing research in the field of hyperpolarisation is motivated by *in vivo* applications, where hyperpolarised compounds are used as magnetic resonance imaging contrast agents.<sup>23</sup> Mostly, this involves transferring the nuclear spin polarisation after hydrogenation to other nuclei (<sup>13</sup>C, <sup>15</sup>N, <sup>31</sup>P) with lower magnetogyric ratios, where spin-lattice relaxation times are longer.<sup>31,47,48</sup> Many of these approaches use zero or very low magnetic fields for hydrogenation and polarisation transfer. This has the advantage that near magnetic equivalence between the two added protons is maintained through the reaction, leading to longer lifetimes.<sup>27–32,49,50</sup> The present work opens a complementary strategy, in that the hydrogenation is done at high field. Deleterious effects of relaxation are minimised by the proximity of the site of hydrogenation to the point of use. Arguably, this approach has advantages in the context of microfluidic systems, where only small quantities of hyperpolarised agents are needed. It may also be possible to adapt the present approach to the SABRE variant of parahydrogen-induced hyperpolarisation.<sup>22</sup> In this context, microfluidic recirculation may enable hyperpolarisation of very small total sample volumes.

## Conclusions

The combination of a highly efficient transmission-line NMR micro detector with parahydrogen-induced hyperpolarisation leads to an unprecedented sensitivity in inductively detected NMR, with a mass limit of detection around 2.2 pmol  $\sqrt{s}$ . This corresponds to a concentration sensitivity of less than 1  $\mu\text{M} \sqrt{s}$ , which, to our knowledge, has not previously been reached at the volume scale of 2.5  $\mu\text{L}$ . This opens the perspective to be able to study chemical processes involving low-abundance species in mass-limited samples. Obviously, such applications require preparation of a hyperpolarised reactant. As the foregoing study shows, the necessary chemistry can be integrated in a microfluidic system. It should be noted that we have used parahydrogen enriched to 50% (compared to 25% at thermal equilibrium); the sensitivity could

easily be boosted by a factor of three by using pure parahydrogen. Microfluidic systems hold great potential in combination with hyperpolarised NMR. All hyperpolarisation techniques require coordinated manipulation of fluids and spin transformations. The results shown in the foregoing demonstrate that in the case of parahydrogen-induced polarisation, this can be assisted considerably by integrating some of the necessary chemical steps on a microfluidic chip. Parahydrogen can be delivered to a reactive solution through a PDMS membrane at sufficient rate to achieve significant levels of hyperpolarisation; dissolution and transport of hydrogen in PDMS does not appear to lead to significant ortho-para equilibration. The highly stable continuous operation of the PHIP@chip system allows quantitative studies of the hydrogenation kinetics, and the relevant relaxation processes. This is demonstrated by the dependence of the steady-state signal intensity on flow rate and the recovery of the hyperpolarised signal after saturation (Fig. 5). Detailed kinetic and transport models, taking into account the deprotection of the catalyst, hydrogen dissolution in the flowing liquid, the hydrogenation reaction, and spin-lattice relaxation, are currently being developed in our laboratory and will be reported on a separate occasion.

The successful demonstration of PHIP on a chip opens important perspectives. Conditions can be optimised for continued production of hyperpolarised metabolites, which opens the possibility to conduct in-situ metabolic studies in microfluidic cultures of cells, tissues, and organisms. While the hyperpolarised compound used here, allyl acetate, is not a metabolite per se, the production of hyperpolarised metabolic species through PHIP has been demonstrated before.<sup>23,30,32,51–53</sup> Some metabolites, such as fumarate, can be generated directly by hydrogenation of an unsaturated precursor.<sup>52</sup> Aime et al. have proposed a more generally applicable method,<sup>51</sup> which relies on the metabolite bound to an alkyne sidearm through an ester linkage. After hydrogenation, the polarisation is transferred to a  $^{13}\text{C}$  nucleus in the metabolic moiety, and the sidearm is cleaved. PHIP@chip opens the possibility of implementing these additional production steps on the same chip. While previous demonstrations of sidearm hydrogenation have been carried out at low magnetic field, it may be possible to adapt recently developed efficient methods for heteronuclear polarisation transfer at high field<sup>33</sup> to this purpose. In turn, this may enable integration of the hyperpolarised metabolite generation with an on-chip culture of

cells or other biological systems. Thanks to its stability, the setup provides a convenient means to optimise pulse sequences and reaction conditions for producing hyperpolarised targets.

## Acknowledgement

This work has been supported by the UK Engineering and Physical Sciences Research Council (EPSRC) and Bruker UK Ltd. in the the form of a CASE conversion studentship for JE. Parts of the work presented here were supported by the European Union Horizon 2020 Future and Emerging Technologies programme (TISuMR project, grant number 737043).

## Supporting Information Available

The following files are available free of charge. The supporting information contains a schematic of the PHIP@chip setup, a fully assigned spectrum (obtained with thermal H<sub>2</sub>), data on the ortho-para conversion of Hydrogen dissolved in PDMS, details of the finite element simulations, the saturation recovery data at all flow rates, and phase-sensitive plots of the simulated and experimental PH-TOCSY spectra.

## References

- (1) (a) Maiwald, M.; Fischer, H. H.; Kim, Y.-K.; Albert, K.; Hasse, H. Quantitative high-resolution online NMR spectroscopy in pharmaceutical reaction and process monitoring. *J. Magn. Reson.* **2004**, *166*, 135–146; (b) Foley, D. A.; Bez, E.; Codina, A.; Colson, K. L.; Fey, M.; Krull, R.; Piroli, D.; Zell, M. T.; Marquez, B. L. NMR Flow Tube for Online NMR Reaction Monitoring. *Analytical chemistry* **2014**, *86*, 12008–12013; (c) Oosthoek-de Vries, A. J.; Nieuwland, P. J.; Bart, J.; Koch, K.; Janssen, J. W. G.; van Bentum, P. J. M.; Rutjes, F. P. J. T.; Gardeniers, H. J. G. E.; Kentgens, A. P. M. Inline Reaction Monitoring of Amine-Catalyzed Acetylation of Benzyl Alcohol Using a Microfluidic Stripline Nuclear Magnetic Resonance Setup. *Journal of the American Chemical Society* **2019**, *141*, 5369–5380, PMID: 30864795.

- (2) (a) Wishart, D. S. Quantitative metabolomics using NMR. *TrAC Trends in Analytical Chemistry* **2008**, *27*, 228–237; (b) Gottschalk, M.; Ivanova, G.; Collins, D. M.; Eustace, A.; O'Connor, R.; Brougham, D. F. Metabolomic studies of human lung carcinoma cell lines using in vitro <sup>1</sup>H-NMR of whole cells and cellular extracts. *NMR in Biomedicine* **2008**, *21*, 809–819; (c) Cuperlovic-Culf, M.; Barnett, D. A.; Culf, A. S.; Chute, I. Cell culture metabolomics: applications and future directions. *Drug Discovery Today* **2010**, *15*, 610–621; (d) Shintu, L.; Baudoin, R.; Navratil, V.; Prot, J.-M.; Pontoizeau, C.; Defernez, M.; Blaise, B. J.; Domange, C.; Péry, A. R.; Toulhoat, P.; Legalais, C.; Brochot, C.; Leclerc, E.; Dumas, M.-E. Metabolomics-on-a-Chip and Predictive Systems Toxicology in Microfluidic Bioartificial Organs. *Analytical Chemistry* **2012**, *84*, 1840–1848.
- (3) Olson, D.; Peck, T.; Webb, A.; Magin, R.; Sweedler, J. High-Resolution Microcoil <sup>1</sup>H-NMR for Mass-Limited, Nanoliter-Volume Samples. *Science* **1995**, *270*, 1967–1970.
- (4) Bart, J.; Kolkman, A. J.; Oosthoek-de Vries, A. J.; Koch, K.; Nieuwland, P. J.; Janssen, H. J. W. G.; van Bentum, P. J. M.; Ampt, K. A. M.; Rutjes, F. P. J. T.; Wijmenga, S. S.; Gardeniers, H. J. G. E.; Kentgens, A. P. M. A Microfluidic High-Resolution NMR Flow Probe. *J Am Chem Soc* **2009**, *131*, 5014–5015.
- (5) Finch, G.; Yilmaz, A.; Utz, M. An optimised detector for in-situ high-resolution NMR in microfluidic devices. *Journal of Magnetic Resonance* **2016**, *262*, 73–80.
- (6) (a) Wang, J.; Sui, G.; Mocharla, V. P.; Lin, R. J.; Phelps, M. E.; Kolb, H. C.; Tseng, H.-R. Integrated Microfluidics for Parallel Screening of an In Situ Click Chemistry Library. *Angew. Chem.* **2006**, *118*, 5402–5407; (b) Theberge, A. B.; Mayot, E.; El Harrak, A.; Kleinschmidt, F.; Huck, W. T. S.; Griffiths, A. D. Microfluidic platform for combinatorial synthesis in picolitre droplets. *Lab Chip* **2012**, *12*, 1320–1326; (c) Hoang, P. H.; Nguyen, C. T.; Perumal, J.; Kim, D.-P. Droplet synthesis of well-defined block copolymers using solvent-resistant microfluidic device. *Lab Chip* **2011**, *11*, 329–335; (d) Ohno, K. i.; Tachikawa, K.; Manz, A. Microfluidics: Applications for analytical purposes in chemistry and biochemistry. *Electrophoresis* **2008**, *29*, 4443–4453;

- (e) Zhou, X.; Cai, S.; Hong, A.; You, Q.; Yu, P.; Sheng, N.; Srivannavit, O.; Muranjan, S.; Rouillard, J. M.; Xia, Y. Microfluidic PicoArray synthesis of oligodeoxynucleotides and simultaneous assembling of multiple DNA sequences. *Nucleic acids research* **2004**, *32*, 5409–5417; (f) Fang, H.; Sun, Y.; Wang, X.; Sharma, M.; Chen, Z.; Cao, X.; Utz, M.; Tian, Z. Probing the kinetics in supramolecular chemistry and molecular assembly by microfluidic-NMR spectroscopy. *Sci. China Chem.* **2018**, *61*, 1460–1464; (g) Hoang, P. H.; Park, H.; Kim, D.-P. Ultrafast and Continuous Synthesis of Unaccommodating Inorganic Nanomaterials in Droplet- and Ionic Liquid-Assisted Microfluidic System. *J Am Chem Soc* **2011**, *133*, 14765–14770; (h) Günther, A.; Jensen, K. Multi-phase microfluidics: from flow characteristics to chemical and materials synthesis. *Lab Chip* **2006**, *6*, 1487–1503.
- (7) (a) Manz, A.; Graber, N.; WIDMER, H. Miniaturized Total Chemical-Analysis Systems - a Novel Concept for Chemical Sensing. *Sensor Actuat B-Chem* **1990**, *1*, 244–248; (b) Whitesides, G. M. The origins and the future of microfluidics. *Nature* **2006**, *442*, 368–373; (c) El-Ali, J.; Sorger, P. K.; Jensen, K. F. Cells on chips. *Nature* **2006**, *442*, 403–411; (d) West, J.; Becker, M.; Tombrink, S.; Manz, A. Micro Total Analysis Systems: Latest Achievements. *Analytical chemistry* **2008**, *80*, 4403–4419; (e) Neužil, P.; Giselbrecht, S.; Länge, K.; Huang, T. J.; Manz, A. Revisiting lab-on-a-chip technology for drug discovery. *Nature Reviews Drug Discovery* **2012**, *11*, 620–632; (f) Gracz, A. D.; Williamson, I. A.; Roche, K. C.; Johnston, M. J.; Wang, F.; Wang, Y.; Attayek, P. J.; Balowski, J.; Liu, X. F.; Laurenza, R. J.; Gaynor, L. T.; Sims, C. E.; Galanko, J. A.; Li, L.; Allbritton, N. L.; Magness, S. T. A high-throughput platform for stem cell niche co-cultures and downstream gene expression analysis. *Nature Cell Biology* **2015**, *17*, 340–349.
- (8) Ryan, H.; Song, S.-H.; Zaß, A.; Korvink, J.; Utz, M. Contactless NMR Spectroscopy on a Chip. *Anal. Chem* **2012**, *84*, 3696–3702.
- (9) Badilita, V.; Meier, R. C.; Spengler, N.; Wallrabe, U.; Utz, M.; Korvink, J. G. Microscale nuclear magnetic resonance: a tool for soft matter research. *Soft Matter* **2012**, *8*, 10583–10597.

- (10) Spengler, N.; Moazenzadeh, A.; Meier, R. C.; Badilita, V.; Korvink, J. G.; Wallrabe, U. Micro-fabricated Helmholtz coil featuring disposable microfluidic sample inserts for applications in nuclear magnetic resonance. *J. Micromech. Microeng.* **2014**, *24*, 034004.
- (11) Sharma, M.; Utz, M. Modular Transmission Line Probes for Microfluidic Nuclear Magnetic Resonance Spectroscopy and Imaging. *Journal of Magnetic Resonance* **2019**, *303*, 75–81.
- (12) (a) Rugar, D.; Yannoni, C. S.; Sidles, J. Mechanical detection of magnetic resonance. *Nature* **1992**, *360*, 563–566; (b) Rugar, D.; Budakian, R.; Mamin, H. J.; Chui, B. W. Single spin detection by magnetic resonance force microscopy. *Nature* **2004**, *430*, 329–332; (c) Mamin, H. J.; Poggio, M.; Degen, C. L.; Rugar, D. Nuclear magnetic resonance imaging with 90-nm resolution. *Nature Nanotech* **2007**, *2*, 301–306; (d) Poggio, M.; Degen, C. L. Force-detected nuclear magnetic resonance: recent advances and future challenges. *Nanotechnology* **2010**, *21*, 342001; (e) Maze, J. R.; Stanwix, P. L.; Hodges, J. S.; Hong, S.; Taylor, J. M.; Cappellaro, P.; Jiang, L.; Dutt, M. V. G.; Togan, E.; Zibrov, A. S.; Yacoby, A.; Walsworth, R. L.; Lukin, M. D. Nanoscale magnetic sensing with an individual electronic spin in diamond. *Nature* **2008**, *455*, 644–647; (f) Staudacher, T.; Shi, F.; Pezzagna, S.; Meijer, J.; Du, J.; Meriles, C. A.; Reinhard, F.; Wrachtrup, J. Nuclear Magnetic Resonance Spectroscopy on a (5-Nanometer)<sup>3</sup> Sample Volume. *Science* **2013**, *339*, 561–563; (g) Rugar, D.; Mamin, H. J.; Sherwood, M. H.; Kim, M.; Rettner, C. T.; Ohno, K.; Awschalom, D. D. Proton magnetic resonance imaging using a nitrogen–vacancy spin sensor. *Nature Nanotech* **2015**, *10*, 120–124; (h) McDermott, R.; Trabesinger, A. H.; Mück, M.; Hahn, E. L.; Pines, A.; Clarke, J. Liquid-State NMR and Scalar Couplings in Microtesla Magnetic Fields. *Science* **2002**, *295*, 2247–2249; (i) Budker, D.; Romalis, M. Optical magnetometry. *NATURE PHYSICS* **2007**, *3*, 227–234; (j) Xu, S.; Yashchuk, V. V.; Donaldson, M. H.; Rochester, S. M.; Budker, D.; Pines, A. Magnetic resonance imaging with an optical atomic magnetometer. *Proceedings of the National Academy of Sciences* **2006**, *103*, 12668–12671; (k) Blanchard, J. W.; Ledbetter, M. P.; Theis, T.; Butler, M. C.; Budker, D.; Pines, A. High-Resolution Zero-Field NMR J-Spectroscopy of Aromatic Compounds. *J Am Chem Soc* **2013**, *135*, 3607–3612.

- (13) Glenn, D. R.; Bucher, D. B.; Lee, J.; Lukin, M. D.; Park, H.; Walsworth, R. L. High-resolution magnetic resonance spectroscopy using a solid-state spin sensor. *Nature* **2018**, *555*, 351–354.
- (14) Münnemann, K.; Spiess, H. W. Nuclear magnetic resonance: The art of signal enhancement. *Nature Physics* **2011**, *7*, 522.
- (15) McDonnell, E.; Han, S.; Hilty, C.; Pierce, K.; Pines, A. NMR analysis on microfluidic devices by remote detection. *Anal. Chem* **2005**, *77*, 8109–8114.
- (16) Desvaux, H.; Marion, D. J. Y.; Huber, G.; Berthault, P. Nuclear Spin-Noise Spectra of Hyperpolarized Systems. *Angewandte Chemie International Edition* **2009**, *48*, 4341–4343.
- (17) Telkki, V.-V.; Zhivonitko, V. V.; Ahola, S.; Kovtunov, K. V.; Jokisaari, J.; Kopytug, I. V. Microfluidic Gas-Flow Imaging Utilizing Parahydrogen-Induced Polarization and Remote-Detection NMR. *Angewandte Chemie International Edition* **2010**, *49*, 8363–8366.
- (18) Paciok, E.; Blümich, B. Ultrafast Microscopy of Microfluidics: Compressed Sensing and Remote Detection. *ANGEWANDTE CHEMIE-INTERNATIONAL EDITION IN ENGLISH-* **2011**, *50*, 5258–5260.
- (19) Jiménez-Martínez, R.; Kennedy, D. J.; Rosenbluh, M.; Donley, E. A.; Knappe, S.; Seltzer, S. J.; Ring, H. L.; Bajaj, V. S.; Kitching, J. Optical hyperpolarization and NMR detection of  $^{129}\text{Xe}$  on a microfluidic chip. *Nature Communications* **2014**, *5*, 3908.
- (20) Causier, A.; Carret, G.; Boutin, C.; Berthelot, T.; Berthault, P. 3D-printed system optimizing dissolution of hyperpolarized gaseous species for micro-sized NMR. *Lab Chip* **2015**, *15*, 2049–2054.
- (21) Hale, W.; Eills, J.; Rossetto, M.; Levitt, M.; Utz, M. PHIP on a Chip - Hyperpolarisation in microfluidic NMR. Oral presentation, Euromar conference, Nantes. 2018.

- (22) Bordonali, L.; Nordin, N.; Fuhrer, E.; MacKinnon, N.; Korvink, J. G. Parahydrogen based NMR hyperpolarisation goes micro: an alveolus for small molecule chemosensing. *Lab Chip* **2019**, *19*, 503–512.
- (23) Hövener, J.-B.; Pravdivtsev, A. N.; Kidd, B.; Bowers, C. R.; Glöggler, S.; Kovtunov, K. V.; Plaumann, M.; Katz-Brull, R.; Buckenmaier, K.; Jerschow, A.; Reineri, F.; Theis, T.; Shchepin, R. V.; Wagner, S.; Bhattacharya, P.; Zacharias, N. M.; Chekmenev, E. Y. Parahydrogen-Based Hyperpolarization for Biomedicine. *Angewandte Chemie International Edition* **2018**, *57*, 11140–11162.
- (24) Duckett, S. B.; Mewis, R. E. Application of Para hydrogen Induced Polarization Techniques in NMR Spectroscopy and Imaging. *Accounts of chemical research* **2012**, *45*, 1247–1257.
- (25) Glöggler, S.; Colell, J.; Appelt, S. Para-hydrogen perspectives in hyperpolarized NMR. *Journal of Magnetic Resonance* **2013**, *235*, 130–142.
- (26) Green, R. A.; Adams, R. W.; Duckett, S. B.; Mewis, R. E.; Williamson, D. C.; Green, G. G. The theory and practice of hyperpolarization in magnetic resonance using parahydrogen. *Progress in nuclear magnetic resonance spectroscopy* **2012**, 1–48.
- (27) Bhattacharya, P.; Chekmenev, E. Y.; Perman, W. H.; Harris, K. C.; Lin, A. P.; Norton, V. A.; Tan, C. T.; Ross, B. D.; Weitekamp, D. P. Towards hyperpolarized <sup>13</sup>C-succinate imaging of brain cancer. *Journal of magnetic resonance* **2007**, *186*, 150–155.
- (28) Chekmenev, E. Y.; Hövener, J.; Norton, V. A.; Harris, K.; Batchelder, L. S.; Bhattacharya, P.; Ross, B. D.; Weitekamp, D. P. PASADENA hyperpolarization of succinic acid for MRI and NMR spectroscopy. *Journal of the American Chemical Society* **2008**, *130*, 4212–4213.
- (29) Chekmenev, E. Y.; Norton, V. A.; Weitekamp, D. P.; Bhattacharya, P. Hyperpolarized <sup>1</sup>H NMR employing low  $\gamma$  nucleus for spin polarization storage. *Journal of the American Chemical Society* **2009**, *131*, 3164–3165.



- (30) Shchepin, R. V.; Coffey, A. M.; Waddell, K. W.; Chekmenev, E. Y. Parahydrogen Induced Polarization of 1-<sup>13</sup>C-Phospholactate-d<sub>2</sub> for Biomedical Imaging with > 30,000,000-fold NMR Signal Enhancement in Water. *Analytical chemistry* **2014**, *86*, 5601–5605.
- (31) Reineri, F.; Boi, T.; Aime, S. ParaHydrogen Induced Polarization of <sup>13</sup>C carboxylate resonance in acetate and pyruvate. *Nature Communications* **2015**, *6*, 5858.
- (32) Cavallari, E.; Carrera, C.; Sorge, M.; Bonne, G.; Muchir, A.; Aime, S.; Reineri, F. The <sup>13</sup>C hyperpolarized pyruvate generated by ParaHydrogen detects the response of the heart to altered metabolism in real time. *Scientific reports* **2018**, *8*, 8366.
- (33) Eills, J.; Stevanato, G.; Bengs, C.; Glöggler, S.; Elliott, S. J.; Alonso-Valdesueiro, J.; Pileio, G.; Levitt, M. H. Singlet order conversion and parahydrogen-induced hyperpolarization of <sup>13</sup>C nuclei in near-equivalent spin systems. *Journal of Magnetic Resonance* **2017**, *274*, 163–172.
- (34) Roth, M.; Kindervater, P.; Raich, H. P.; Bargon, J.; Spiess, H. W.; Münnemann, K. Continuous <sup>1</sup>H and <sup>13</sup>C Signal Enhancement in NMR Spectroscopy and MRI Using Parahydrogen and Hollow-Fiber Membranes. *Angew. Chem.* **2010**, *122*, 8536–8540.
- (35) Lehmkuhl, S.; Wiese, M.; Schubert, L.; Held, M.; Küppers, M.; Wessling, M.; Blümich, B. Continuous hyperpolarization with parahydrogen in a membrane reactor. *Journal of Magnetic Resonance* **2018**, *291*, 8–13.
- (36) Giraudeau, P.; Shrot, Y.; Frydman, L. Multiple Ultrafast, Broadband 2D NMR Spectra of Hyperpolarized Natural Products. *J Am Chem Soc* **2009**, *131*, 13902–13903.
- (37) Lloyd, L. S.; Adams, R. W.; Bernstein, M.; Coombes, S.; Duckett, S. B.; Green, G. G. R.; Lewis, R. J.; Mewis, R. E.; Sleigh, C. J. Utilization of SABRE-Derived Hyperpolarization To Detect Low-Concentration Analytes via 1D and 2D NMR Methods. *J Am Chem Soc* **2012**, *134*, 12904–12907.
- (38) Eshuis, N.; Aspers, R. L. E. G.; van Weerdenburg, B. J. A.; Feiters, M. C.; Rutjes, F. P. J. T.; Wijmenga, S. S.; Tessari, M. 2D NMR Trace Analysis by Continuous Hyperpolarization at High Magnetic Field. *Angew. Chem.* **2015**, *127*, 14735–14738.

- (39) Yilmaz, A.; Utz, M. Characterisation of oxygen permeation into a microfluidic device for cell culture by in situ NMR spectroscopy. *Lab Chip* **2016**, *16*, 2079–2085.
- (40) Bezanson, J.; Edelman, A.; Karpinski, S.; Shah, V. B. Julia: A Fresh Approach to Numerical Computing. *SIAM Rev.* **2017**, *59*, 65–98.
- (41) Cavallari, E.; Carrera, C.; Boi, T.; Aime, S.; Reineri, F. Effects of magnetic field cycle on the polarization transfer from parahydrogen to heteronuclei through long-range J-couplings. *The Journal of Physical Chemistry B* **2015**, *119*, 10035–10041.
- (42) Mompeán, M.; Sánchez-Donoso, R. M.; Hoz, A.; Saggiomo, V.; Velders, A. H.; Gomez, M. V. Pushing nuclear magnetic resonance sensitivity limits with microfluidics and photo-chemically induced dynamic nuclear polarization. *Nature communications* **2018**, *9*, 108.
- (43) Zalesskiy, S. S.; Danieli, E.; Blümich, B.; Ananikov, V. P. Miniaturization of NMR Systems: Desktop Spectrometers, Microcoil Spectroscopy, and “NMR on a Chip” for Chemistry, Biochemistry, and Industry. *Chem. Rev* **2014**, *114*, 5641–5694.
- (44) Mishkovsky, M.; Frydman, L. Progress in Hyperpolarized Ultrafast 2D NMR Spectroscopy. *Chemphyschem* **2008**, *9*, 2340–2348.
- (45) Kiryutin, A. S.; Sauer, G.; Tietze, D.; Brodrecht, M.; Knecht, S.; Yurkovskaya, A. V.; Ivanov, K. L.; Avrutina, O.; Kolmar, H.; Buntkowsky, G. Ultrafast Single-Scan 2D NMR Spectroscopic Detection of a PHIP-Hyperpolarized Protease Inhibitor. *Chemistry - A European Journal* **2019**, *32*, 211–7.
- (46) (a) Levitt, M. H.; Freeman, R.; Frenkiel, T. Supercycles for Broadband Heteronuclear Decoupling. *Journal of Magnetic Resonance (1969)* **1982**, *50*, 157–160; (b) Bax, A.; Davis, D. G. MLEV-17-Based Two-Dimensional Homonuclear Magnetization Transfer Spectroscopy. *Journal of Magnetic Resonance (1969)* **1985**, *65*, 355–360.
- (47) Goldman, M.; Johannesson, H.; Axelsson, O.; Karlsson, M. Hyperpolarization of <sup>13</sup>C through order transfer from parahydrogen: A new contrast agent for MRI. *Magn Reson Imaging* **2005**, *23*, 153–157.

- (48) Goldman, M.; Johannesson, H.; Axelsson, O.; Karlsson, M. Design and implementation of  $^{13}\text{C}$  hyper polarization from para-hydrogen, for new MRI contrast agents. *Comptes Rendus Chimie* **2006**, *9*, 357–363.
- (49) Ripka, B.; Eills, J.; Kouřilová, H.; Leutzsch, M.; H. Levitt, M.; Münnemann, K. Hyperpolarized Fumarate via Parahydrogen. *Chemical Communications* **2018**, *54*, 12246–12249.
- (50) Roy, S. S.; Appleby, K. M.; Fear, E. J.; Duckett, S. B. SABRE-Relay: A Versatile Route to Hyperpolarization. *The journal of physical chemistry letters* **2018**, *9*, 1112–1117.
- (51) Reineri, F.; Boi, T.; Aime, S. Parahydrogen induced polarization of  $^{13}\text{C}$  carboxylate resonance in acetate and pyruvate. *Nature communications* **2015**, *6*, 5858.
- (52) Ripka, B.; Eills, J.; Kouřilová, H.; Leutzsch, M.; Levitt, M. H.; Münnemann, K. Hyperpolarized fumarate via parahydrogen. *Chem. Commun.* **2018**, *54*, 12246–12249.
- (53) Korchak, S.; Yang, S.; Mamone, S.; Glögler, S. Pulsed Magnetic Resonance to Signal-Enhance Metabolites within Seconds by utilizing para-Hydrogen. *ChemistryOpen* **2018**, *7*, 344–348.